JOURNAL OF SYNCHROTRON RADIATION

ISSN 1600-5775

Received 7 January 2020
Accepted 15 May 2020

Edited by M. Yabashi, RIKEN SPring-8 Center, Japan

Keywords: free-electron lasers; soft X-rays; spectrometers; variable-line-spacing gratings; ray tracing.

Design of an online spectrometer for the diagnosis of free-electron lasers

Ximing Zhang,[a,b] Zhi Guo,[a,c]* Xiangyu Meng,[a,c] Jiahua Chen,[a,c] Zhan Ji,[a,c] Zuanming Jin,[b] Xiangzhi Zhang,[a,c] Yong Wang[a,c] and Renzhong Tai[a,c]*

[a]Shanghai Institute of Applied Physics, Chinese Academy of Sciences, 2019 Jialuo Highway, Jiading District, Shanghai 201800, People's Republic of China, [b]Shanghai University, 99 Shangda Road, Baoshan District, Shanghai 200444, People's Republic of China, and [c]Shanghai Advanced Research Institute, Chinese Academy of Sciences, 239 Zhangheng Road, Pudong District, Shanghai 201204, People's Republic of China. *Correspondence e-mail: guozhi@zjlab.org.cn, tairenzhong@zjlab.org.cn

A self-amplified spontaneous emission free-electron laser (FEL) is under construction at the Shanghai Soft X-ray Free-Electron Facility. Therefore, it is necessary to develop a suitable diagnostic tool capable of resolving the natural emission band of each FEL pulse. Thus, an online spectrometer with a plane mirror and plane variable-line-spacing grating at grazing incidence to monitor each single FEL pulse during the propagation of FEL radiation has been designed and is presented in this work. The method of ray tracing is used for monitoring incident radiation in order to understand spectral characteristics, and *SHADOW*, an X-ray optics simulation tool, and *SRW*, an X-ray optics wavefront tool, are applied to study the resolving power and focusing properties of the grating. The designed resolving power is $\sim 3 \times 10^4$ at 620 eV. Meanwhile, the effect of the actual slope error of mirrors on the ray-tracing results is also discussed. In order to provide further optimization for the choice of grating, a comparison of resolving powers between 2000 lines mm^{-1} and 3000 lines mm^{-1} gratings at different energies is analyzed in detail and radiation damage of mirrors as well as parameters such as the first-order diffraction angle β, the exit-arm length r_2, and the tilt angle θ between the focal plane and the diffraction arm are studied and optimized. This work has provided comprehensive designing methods and detailed data for the design of diagnostic spectrometers in soft X-ray FELs and will be favorable to the design of other similar instruments.

1. Introduction

The free-electron laser (FEL), which is based on the principle of self-amplified spontaneous emission (SASE), is of great importance in the extreme ultraviolet and soft X-ray region. For instance, FELs have many unique properties, such as transversely coherent and ultrashort-pulsed sources, high brightness and peak power, tunable wavelengths, and wide spectral ranges (Saldin *et al.*, 1995; Tiedtke *et al.*, 2004; Amann *et al.*, 2012; Allaria *et al.*, 2012; Togashi *et al.*, 2013; McNeil *et al.*, 2010; Emma *et al.*, 2010). The above-mentioned facts show a promising prospect for utilizing FELs in various fields of physics; therefore, FELs will surely create a new era in studying the interaction between soft X-ray radiation and matter and single-particle imaging (Ayvazyan *et al.*, 2006).

In a SASE FEL, the output radiation first starts from spontaneous emission in the electron beam, followed by an amplification process in which the radiation grows exponentially when passing through a long undulator (Saldin *et al.*, 1995). As a result, the characteristics of the emitted radiation are not as stable as the high-gain harmonic generation mode, especially for each single FEL pulse. These pulses are different

in some respects, such as intensity, temporal structure and spectral distribution. Consequently, it is necessary to develop a suitable diagnostic tool that will be capable of resolving the natural emission band of each FEL pulse so that the characteristics of FEL radiation can be studied and the measurements of the FEL radiation can be highly reliable and precise, which is useful for both experimentalists and machine physicists. At present, several kinds of online grating spectrometers have been designed and applied worldwide (Reininger *et al.*, 2004; Frassetto *et al.*, 2008; Stohr, 2011; Brenner *et al.*, 2011; Li *et al.*, 2015). However, most of them are usually suited for the energy region from 100 to 500 eV rather than the energy region from 800 to 1000 eV.

In this article, we present an online grating spectrometer to monitor each single FEL pulse during the propagation of FEL radiation and measure the shot-by-shot energy profile (Ayvazyan *et al.*, 2002; Makita *et al.*, 2015; Rehanek *et al.*, 2017; Tono *et al.*, 2013). A plane variable-line-spacing (VLS) grating is set up for monitoring the FEL radiation in an almost noninvasive way, as it can disperse a small part of the incoming radiation for further measurement and reflect most of the radiation to the experiment at the same time. Meanwhile, the radiation damage, the ray-tracing results, optimization towards the energy region from 800 to 1000 eV and parameters of the first-order diffraction are discussed in detail. Moreover, comparing with the 2000 lines mm^{-1} grating, a simulation of the spectrometer using the 3000 lines mm^{-1} grating is made for future optimization for the energy region from 800 to 1000 eV. At present, the 2000 lines mm^{-1} grating has been installed and has worked approximately from 100 to 1000 eV but has a lower energy-resolving power for the energy region from 800 to 1000 eV, while the 3000 lines mm^{-1} grating is able to increase the energy-resolving power from 15 000 to 25 000 at 1033 eV according to the simulation.

2. Optics design

The SASE FEL at the Shanghai Soft X-ray Free-Electron Facility (SXFEL) is based on the principle of SASE and is under construction. Simulation values of the SASE XFEL beam on some distinct photon energies from 103 to 1033 eV have been achieved and some values are shown in Table 1.

Table 1
Basic parameters of the undulator beamline (SASE) in the SXFEL.

Photon-energy range (eV)	103–1033
Wavelength range (nm)	1.2–12
Pulse-energy range (μJ)	0.2–398 (0.2 at 1033 eV, 145 at 620 eV, 398 at 103 eV)
Source size (μm)	130 at 620 eV
Divergence angle (μrad)	10.0 at 620 eV
Pulse length (FWHM, fs)	∼117 at 620 eV
Band width (RMS, $\Delta E/E$)	0.06% at 620 eV, 0.04% at 1033 eV, 0.2% at 103 eV
Repetition rate (Hz)	1–50

The main optical layout of the SASE beamline at the SXFEL is presented in Fig. 1. First, the plane mirror PM1 with an incident angle of 88.5° is positioned 59 m downstream of the FEL source and a shielding wall is located downstream of PM1. A plane VLS grating parallel to PM1 is located 65 m downstream of the FEL source, just downstream of the shielding wall. Both the PM1 and the VLS grating are designed with a fixed grazing incidence angle of 88.5° (according to the normal line). The above elements form a spectrometer. Two branches are designed downstream of the diagnostic system. A Kirkpatrick–Baez (K–B) mirror pair (ECM8 and ECM9) can focus the beam to the endstation 1 sample position, which is 120 m downstream of the source. The pink beam transmits through the monochromator and bendable mirror chamber into the K–B mirror pairs and biological imaging endstation. Because of the application of high-quality mirrors (height error < 6 nm, slope error < 0.2 μrad), the coherence and wavefront of the FEL beam can be preserved as far as possible. An alternative monochromatic/pink beam branch (to endstation 2) has been designed for ultrafast physical and chemical experiments that require higher energy-resolving power ($\Delta E/E \simeq 0.01\%$) (Guo *et al.*, 2017; Meng *et al.*, 2019) – this alternative system for monochromatic or pink beam and an ellipsoidal mirror for focusing are not discussed in detail in this article.

The incident SASE FEL radiation passes into PM1 and is reflected at the grating. Coupling of mirrors PM1 and PM2 with the same incidence angle has the function of blocking the direct incidence of the electron beam on the downstream mirrors. A VLS grating exists in the central area of the online

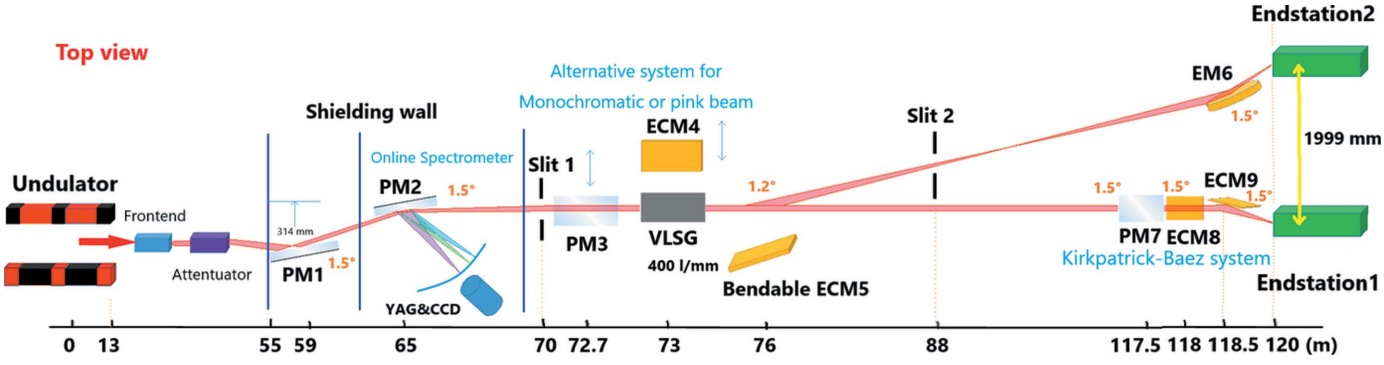

Figure 1
Optical layout of the SASE beamline (all units are in metres).

spectrometer mirror PM2. The grating diffracts the radiation into two parts. One part of the incoming radiation is deflected into the first diffraction order, which only covers a small portion of the reflected beam (∼3%), while the other part is deflected into the zero order and straight forward towards the beamline, and the wavefront can be maintained as far as possible. A shielding wall is located between PM1 and PM2 to block the bremsstrahlung radiation from the FEL. This layout ensures that the FEL radiation propagates as much flux as possible in the modes of zero-order reflection and less than 3% in the first order for the energy spectrum measurement of a single pulse. Moreover, because the FEL radiation pulses with different photon energies differ in diffraction angle β and focal length, a movable charge-coupled device (CCD) camera can be placed at the focal point of the first-order diffraction to record the energy spectrum of a single pulse. In contrast, the angle between the focal plane and propagating direction of first-order diffraction depends on the photon energy variation (Brenner *et al.*, 2011; Svetina *et al.*, 2016; Palutke *et al.*, 2015).

There are two advantages of using a plane VLS grating in an online spectrometer. First, it can focus the dispersive beam onto the CCD camera, which can eliminate a focusing mirror in the dispersive direction. Second, the aberration can be minimized as a result of the optimization of parameters b_2, b_3 and b_4.

The model of the CCD camera used in the beamline is Andor Zyla 4.2 Plus, where the quantum efficiency is 82%, and is optimized for all fluorophores.

3. Working principle of the grating

As a function of the surface position, the grating line-density variation $k(\omega)$ along the VLS grating length is given as a polynomial by

$$k(\omega) = k_0(1 + 2b_2\omega + 3b_3\omega^2 + 4b_4\omega^3\ldots), \tag{1}$$

where k_0 indicates the groove line density at the grating center, ω is the position relative to the grating center, and b_2, b_3 and b_4 are the ruling variation parameters (Noda *et al.*, 1974; Kita *et al.*, 1983; Harada *et al.*, 1999; Reininger *et al.*, 2004).

According to the focusing equations of a VLS grating,

$$\frac{\cos^2\alpha}{r_1} + \frac{\cos^2\beta}{r_2} = 2nb_2k_0\lambda \tag{2}$$

and

$$\sin\alpha - \sin\beta = nk_0\lambda, \tag{3}$$

where α and β represent the incidence and diffraction angles relative to the normal line, respectively, and n, λ, r_1 and r_2 represent the diffraction order, wavelength, object distance and image distance for the VLS grating, respectively.

The diffraction angle β can be expressed as

$$\beta = \arcsin(\sin\alpha - nk_0\lambda). \tag{4}$$

The image distance is given by

$$r_2(\beta) = \frac{\cos^2\beta}{2nb_2k_0\lambda - [(\cos^2\alpha)/r_1]}. \tag{5}$$

The tilt angle between the focal plane and propagating direction of the diffraction beam can be obtained from equations (6) and (7),

$$r_2'(\beta) = \frac{2b_2\cos^3\beta - \sin 2\beta\left\{2b_2(\sin\alpha - \sin\beta) - [(\cos^2\alpha)/r_1]\right\}}{\left\{2b_2(\sin\alpha - \sin\beta) - [(\cos^2\alpha)/r_1]\right\}} \tag{6}$$

and

$$\tan\theta = \frac{r_2(\beta)}{r_2'(\beta)}. \tag{7}$$

Thus, the tilt angle between the focal plane and propagating direction of first-order diffraction can be calculated from equations (5), (6) and (7) as

$$\theta = \arctan\frac{r_2(\beta)}{r_2'(\beta)}. \tag{8}$$

The equations for the focusing formula of grating can be expressed as

$$F_{20} = \frac{\cos^2\alpha}{r_1} + \frac{\cos^2\beta}{r_2} - 2b_2k_on\lambda, \tag{9}$$

$$F_{30} = \sin\alpha\frac{\cos^2\alpha}{r_1^2} + \sin\beta\frac{\cos^2\beta}{r_2^2} + 2b_3k_on\lambda, \tag{10}$$

and

$$F_{40} = \frac{\cos^2\alpha\left(4\sin^2\alpha - \cos^2\alpha\right)}{r_1^3} + \frac{\cos^2\beta\left[4\sin^2(-\beta) - \cos^2\beta\right]}{r_2^3} + 8b_4k_on\lambda, \tag{11}$$

where F_{ij} is the aberration value. Equation (9) is the focusing equation of a VLS grating when the parameter F_{20} is zero, as is shown in equation (2). When designing a spectrometer using an VLS grating, the condition $F_{ij} = 0$ has to be satisfied to obtain completely stigmatic image focusing. However, it is impossible to satisfy the stigmatic condition for the total wavelength range, but every key term of F_{ij} can be zeroed or minimized to reduce aberration (Harada & Kita, 1980). As long as the parameters k_0, α, β, n, r_1, r_2 and λ have been determined, the coefficients b_2, b_3 and b_4 can be calculated to minimize the values of F_{20}, F_{30} and F_{40}. Under the horizontal focal condition, F_{20} can be zeroed in the whole energy region if the values of α and β are selected appropriately so that b_2 can be calculated. For the same reason, b_3 can be calculated if the higher-order aberration value F_{30} is zeroed at a point with specific energy, while F_{40} is too small to be calculated at other energies. Fig. 2 shows a detailed drawing of the ruled area in the center of the VLS grating; thus, it is clear that PM2 is a laminar grating.

The central groove density, incidence angle with respect to the normal line, and entrance-arm length are 2000 lines mm^{-1}, 88.5° and 65 m, respectively. The inside order (first order) is

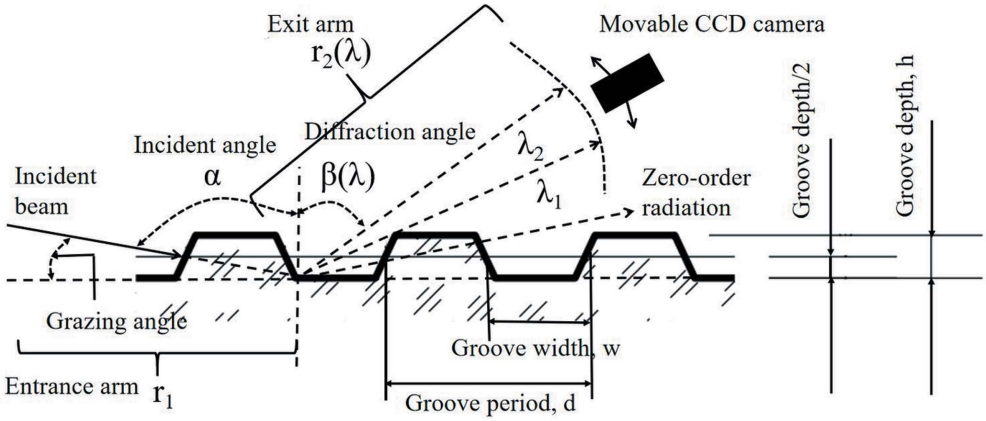

Figure 2
Cross section of the grating ruling area.

selected to obtain higher energy-resolving power and enlarge the included angle between the first-order diffraction line and the directly reflected line (zero order), and the particular wavelength is hc/E, where h is Planck's constant and c is the speed of light in a vacuum. As a result, the focusing parameter, b_2, can be calculated when F_{20} is set equal to 0. The basic design parameters of the VLS grating are listed in Table 2.

The central groove density of the delivered grating is 1999.393 lines mm^{-1}. As Fig. 3(*a*) shows, the groove density varies linearly with the parameter x, where x is defined as the distance from the center of the grating. The measured groove density agrees well with the design data shown in Table 2. Furthermore, the parameters b_2, b_3 and b_4 of the processed grating are measured as $2.718 \times 10^{-4}\,mm^{-1}$, $6.876 \times 10^{-8}\,mm^{-2}$ and $-2.383 \times 10^{-11}\,mm^{-3}$, respectively. The aberration values F_{20}, F_{30} and F_{40} can be calculated from equations (9), (10) and (11), respectively. Fig. 3(*b*) shows the values of F_{20}, F_{30} and F_{40} versus photon energy varying from 100 to 1000 eV. The introduction of appropriate b_2, b_3 and b_4 values can optimize the aberration values F_{20}, F_{30} and F_{40}, which are close to zero and negligible.

A schematic view of the spectrometer is shown in Fig. 4. The incidence angle remains constant at 88.5°, while the diffraction

Table 2
Basic parameters of the VLS grating.

Blank material	Silicon
Substrate dimensions (mm)	300 (length) × 50 (width) × 50 (thickness)
Effective optical dimension (mm)	280 (length) × 40 (width)
Slope error for the surface of the substrate (μrad RMS)	0.2 (meridional direction), 1 (sagittal direction)
Grating dimension (mm)	80 (length) × 5 (width)
Height error of the substrate (peak-to-valley, nm)	<6
Grooving mode	Constant ruling depth, groove depth h = 6 nm ± 10%, ratio of groove width to the spacing w/d = 0.65 ± 10%
Coating (nm)	B_4C 40 ± 10 with Cr binding layer
Coating density (g cm^{-3})	>2.25
Coating thickness (nm)	40 ± 10
Substrate roughness (nm, RMS)	0.3
Ruling density and design values of the ruling variation parameters	$k(\omega) = k_0(1 + 2b_2\omega + 3b_3\omega^2 + 4b_4\omega^3 + \ldots)$ (ω is 0 at the grating center with the units in mm), k_0 = 2000 lines mm^{-1} ± 1.5 (0.075%), $b_2 = 2.714211 \times 10^{-4}\,mm^{-1}$ ± 4.3×10^{-7} (0.16%), $b_3 = 6.72 \times 10^{-8}\,mm^{-2}$ ± 6.7×10^{-9} (10%), $b_4 = -1.7 \times 10^{-11}\,mm^{-3}$ ± 5.1×10^{-12} (30%)

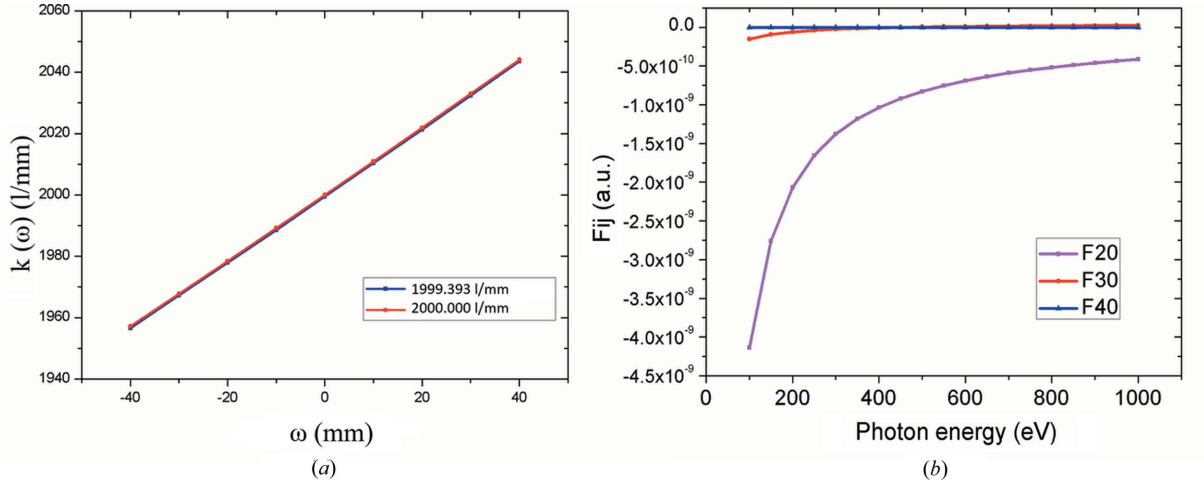

(*a*) (*b*)

Figure 3
Calculated results of (*a*) the groove density at different locations of the grating and (*b*) the aberrations F_{20}, F_{30} and F_{40} versus photon energy varying from 100 to 1000 eV.

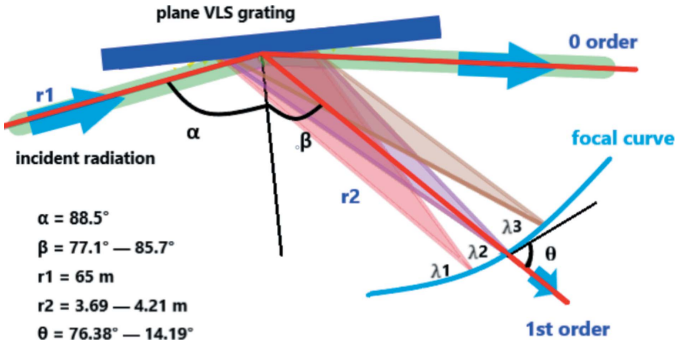

Figure 4
Optical layout of the spectrometer.

angle β and exit-arm length of the spectrometer vary with the incident photon energy. The diffraction angle β ranges from 77.1 to 85.7° with photon energy varying from 100 to 1000 eV. When an energy of 620 eV is selected for optimization, the exit-arm length is 4.005 m.

In addition, to maintain the wavefront and coherence of the incident beam, most of the substrate area is fabricated as a plane mirror with a slope error of 0.1 µrad and a height error of 5 nm. The grating rulings are only etched in the center region, which is ∼80 mm × 5 mm (L × W). Fig. 5 shows a schematic view of the grating surface area.

4. Radiation damage and diffraction efficiency of the grating

The irradiation tolerance of the optical coating materials can be estimated by comparing the absorption dose with the melting threshold dose (Bionta, 2000; Yabashi *et al.*, 2007; Koyama *et al.*, 2016), which is known as $W_{\rm melt} \simeq 3k_{\rm B}T_{\rm melt}$; the melting threshold doses of Au and B_4C are calculated as 0.35 eV atom^{-1} and 0.68 eV atom^{-1}, respectively. B_4C, which is known as a low-Z coating material, has a higher tolerance than a high-Z material such as Au owing to its high melting threshold dose. However, before reaching the melting threshold dose, single atoms may fall off because of the strong irradiation of the FEL pulse; thus, the absorption dose of single atoms is set as the safety threshold to be less than 0.1 eV atom^{-1} to ensure the safety of the coating material.

Meanwhile, when the groove of the grating is irradiated under the grazing-incidence condition, the lateral surface of the groove is nearly irradiated under the normal incidence condition, which leads to serious radiation damage on coating materials on the lateral surface of the groove, as shown in Fig. 6(*a*). Fig. 6(*b*) shows that the energy deposition of Au is 10–30 times more than that of B_4C at energies ranging from 100 to 1000 eV under normal incidence conditions. Except for the energy of ∼200 eV, the absorption dose of the single atoms of B_4C is less than 0.1 eV atom^{-1} (safety threshold dose), which is less than 0.68 eV atom^{-1} (melting threshold dose of B_4C); thus, it is safer to use B_4C as the coating material.

To reduce the risk of damage and deformations on mirrors by the FEL pulse with high peak power, both PM1 and PM2 are coated with B_4C on silicon substrates. The VLS grating of PM2 is holographically recorded and then ion etched inside the substrate.

With most of the radiation in the zero order, the grating profile is determined because every part of the grating surface should make an angle smaller than 1.5° with the incoming radiation; as a result, the first-order efficiency should be within a reasonable range (Reininger *et al.*, 2004). The grating angle has been selected to maintain the energy density well under the damage threshold of the adopted coating (Frassetto *et al.*, 2008). Both the mirror and grating are coated with B_4C because this material is stable and has a high damage threshold. The software *Reflect* (Thompson & Vaughan, 2001) was used to calculate the efficiency for 2000 lines mm^{-1} B_4C-coated grating. Fig. 7 shows the efficiency of the grating with varying photon energy. The efficiency ranges from ∼1 to 20% in the photon-energy range of 100–1000 eV.

As Fig. 7(*a*) shows, the groove ratio between the groove width and period affects the diffraction efficiency. A suitable ratio of 0.65 is chosen because of its relatively higher diffraction efficiency at energies lower than 500 eV. Meanwhile, the diffraction efficiencies at different depths were calculated and a depth of 6 nm was selected based on the consideration of achieving relatively higher efficiency in the full energy range, as shown in Fig. 7(*b*).

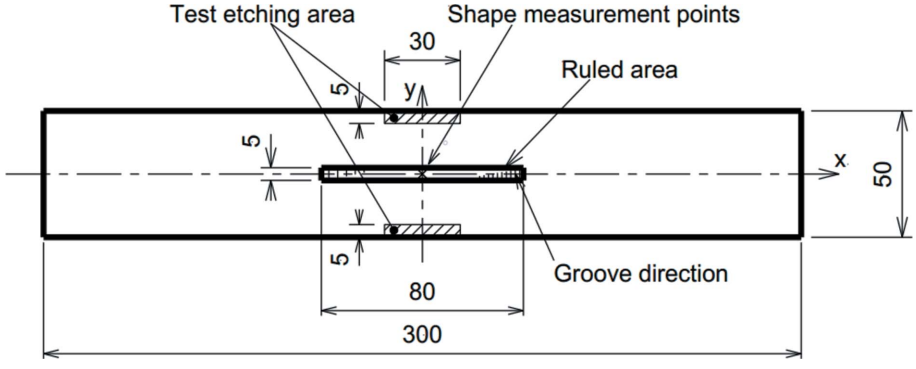

Figure 5
Schematic view of the grating, where the grating rulings are only etched in the center region, which is ∼80 mm × 5 mm (L × W), while the rest of the surface is a plane mirror.

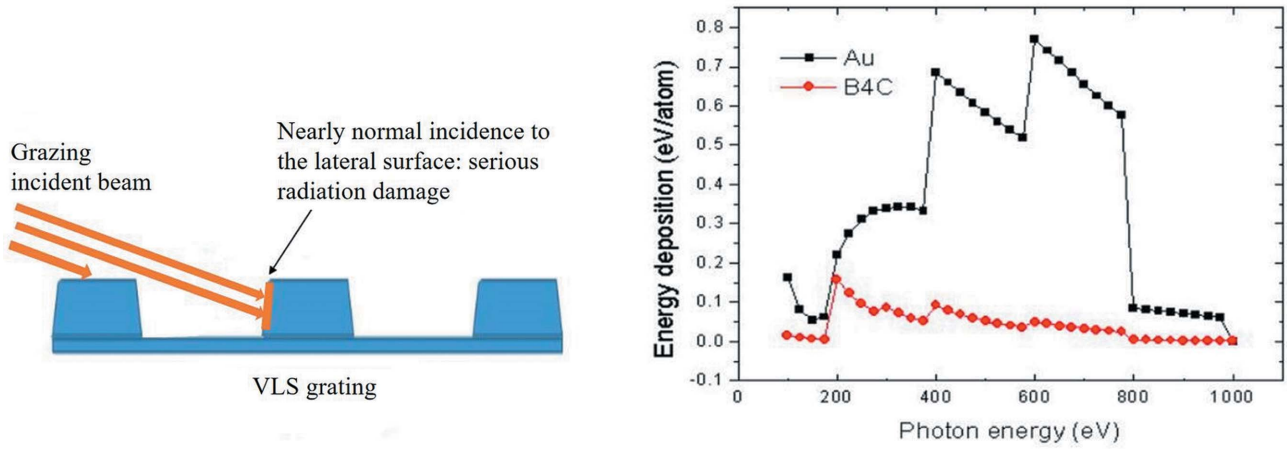

(*a*) (*b*)

Figure 6
(*a*) Schematic of the incident radiation on the lateral surface of the groove of the grating. (*b*) On the lateral surface of the groove of the grating, the energy deposition of PM2 using Au or B_4C as the coating material under normal incidence conditions.

5. Results of ray tracing and wavefront simulation

The FEL pulse has a narrow spectral bandwidth, as shown in Table 1. The precise diagnosis of the spectral profile for each pulse is crucial for the FEL experiments, *e.g.* coherent diffraction imaging, ultrafast X-ray spectroscopy for chemistry and time-resolved X-ray scattering. To understand the spectral characteristics, the ray-tracing method is used for monitoring the incident radiation. Some ray-tracing simulation tools have been applied in the synchrotron and FEL beamline designs, *e.g. RAY*, *SHADOW*, *SRW* (*Synchrotron Radiation Workshop)*, *PHASE*, *HYBRID* and *MOI* (Sanchez del Rio *et al.*, 2011; Bahrdt, 2007; Samoylova *et al.*, 2011; Chubar *et al.*, 2011; Meng *et al.*, 2017). *SHADOW*, an X-ray optics simulation tool, and *SRW*, an X-ray optics wavefront tool, have been implemented in the design of the spectral diagnostic grating in the SASE FEL beamline with the aim of verifying the rationality of the design of the spectrometer and proposing an improvement plan to the energy-resolving power of the energy region from 800 to 1000 eV.

SHADOW can simulate the geometric effects of optical elements, whereas their diffraction contributions are calculated using wavefront propagation. The results from the diffraction and geometric effects are integrated together by numerical convolution and ray re-sampling (Sanchez del Rio *et al.*, 2011; Meng *et al.*, 2017). The *SRW* code, which is based on the Fourier optics approach, calculates the spontaneous emission of electrons through magnetic fields, and simulates the wavefront propagation through optical elements and free space. The multi-electron *SRW* is the most advanced code dealing with partially coherent radiation (Samoylova *et al.*, 2011; Chubar, 2014; Meng *et al.*, 2017).

The main contributions to the resolving power of the spectrum are the source size, entrance- and exit-slit sizes, and mirror slope and height error (Li *et al.*, 2015). For the SASE beamline of the SXFEL, 620 eV (2 nm) is the main optimized photon energy, which is chosen as the main ray-tracing simulation energy. The central groove density of the grating is 1999.4 lines mm^{-1}, while the groove density increases

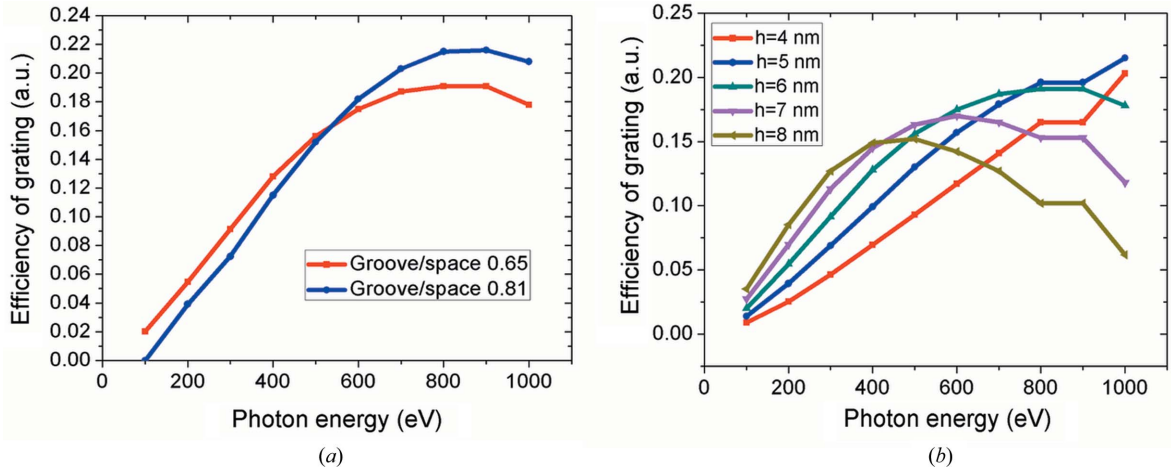

(*a*) (*b*)

Figure 7
The first-order diffraction efficiency of the grating versus photon energy. (*a*) Diffraction efficiencies at different groove ratios of 0.65 or 0.81; (*b*) Diffraction efficiencies at different groove depths from 4 to 8 nm.

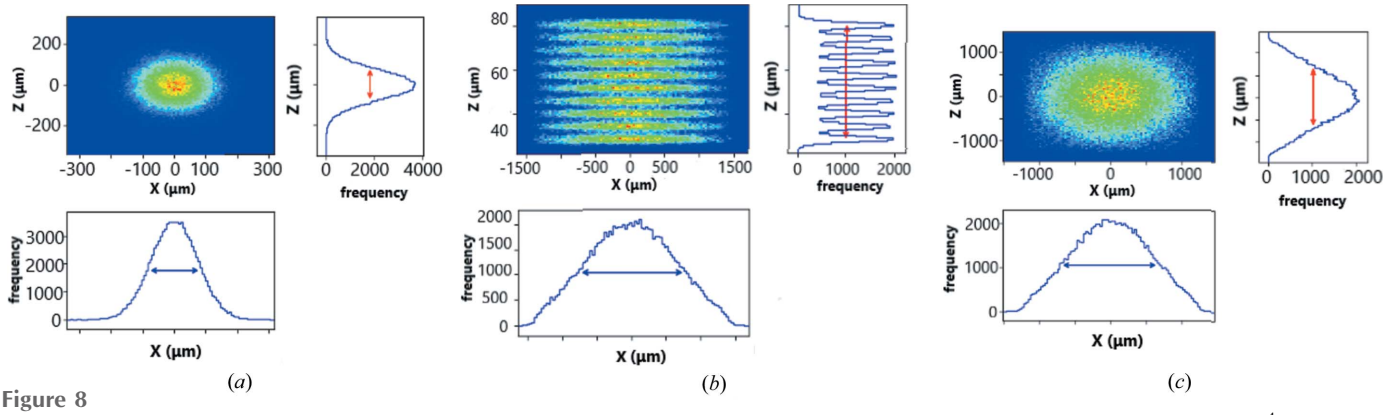

Figure 8
Ray-tracing results at (*a*) the source, (*b*) PM1 and (*c*) the diagnostic grating PM2 at energy 620 eV with a resolving power of 3×10^4 ($E/\Delta E$), as simulated by *SHADOW*.

gradually from 1956 lines mm^{-1} at the upstream side to 2034 lines mm^{-1} at the downstream side. Thus, the dispersed first-order monochromatic beam can be focused on the CCD camera.

Fig. 8 shows the ray-tracing results of the beam cross section at the source, PM1 and diagnostic grating PM2 at an energy of 620 eV. The side profile of the incident-beam intensity is assumed to be Gaussian. The 1σ value of the divergence angle is 10 μrad, with a spot size of 74 μm. Relying on the optimization of the beamline design, the acceptance angle is over 6σ at 620 eV, with the aim of obtaining a higher photon flux and maintaining the wavefront on the sample position. The beam cross section of Gaussian-type radiation is amplified when propagating to PM1, as shown in Fig. 8(*b*). For the diagnostic grating, the energy-resolving power is over 3×10^4 ($E/\Delta E$) at 620 eV. Compared with the 1600 bandwidth ($E/\Delta E$) of the incident pulse, one single pulse can be dispersed to 10–20 distinguishable lines with an interval between two adjacent lines of ∼5 μm at the CCD camera, as shown in Fig. 8(*c*).

Under the same conditions, the tracing results simulated by *SRW* are shown in Fig. 9 and are similar to those simulated by *SHADOW*. Compared with the geometrical model, the *SRW* code is superior in the simulation of coherent X-rays, especially in FEL beamline design. The interval between two adjacent energy lines is ∼5 μm, as shown in Fig. 9. Overall, the *SRW* results agree with the *SHADOW* results.

Fig. 10 presents the tracing results of the 2000 lines mm^{-1} and 3000 lines mm^{-1} VLS gratings in the energy region from 100 to 500 eV (207 and 413 eV, respectively). Both the 2000 lines mm^{-1} and 3000 lines mm^{-1} gratings exhibit an energy-resolving power of over 3×10^4; for instance, the energy-resolving power of the 2000 lines mm^{-1} grating is 5×10^4 at 207 eV and ∼6.5×10^4 for the 3000 lines mm^{-1} grating, where the dispersed monochromatic beam can be distinguished explicitly by these two gratings. However, the energy-resolving power of the 3000 lines mm^{-1} grating is superior to that of the 2000 lines mm^{-1} grating in the energy region from 800 to 1000 eV (827 and 1033 eV, respectively). The energy-resolving power of the 3000 lines mm^{-1} grating can exceed 2.5×10^4 at 1033 eV. In

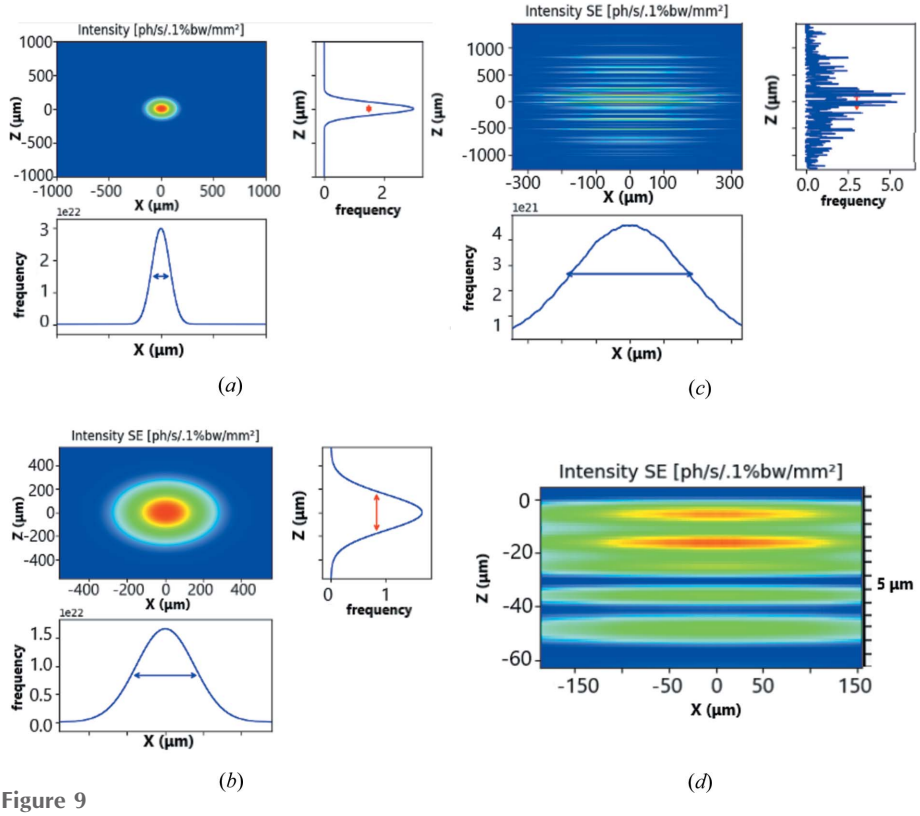

Figure 9
Ray-tracing results at (*a*) the source, (*b*) PM1 and (*c*) the diagnostic grating PM2 at 620 eV with a resolving power of 3×10^4 ($E/\Delta E$), as simulated by *SRW*. (*d*) The interval between two adjacent energy lines is ∼5 μm.

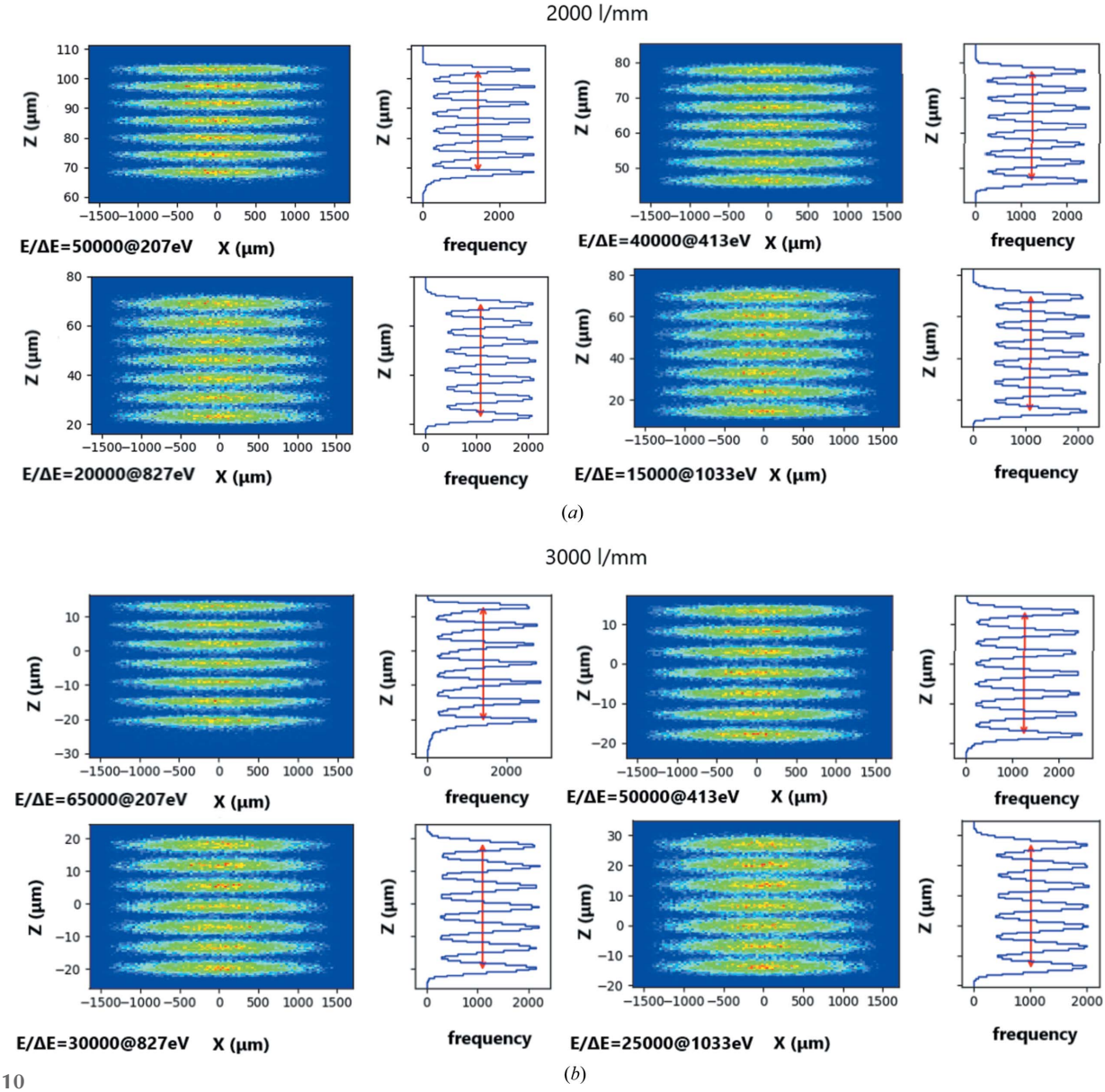

Figure 10
Comparison between (*a*) the 2000 lines mm^{-1} grating and (*b*) the 3000 lines mm^{-1} grating in the energy region from 100 to 500 eV (207 and 413 eV, respectively) and the energy region from 800 to 1000 eV (827 and 1033 eV, respectively) with different resolving powers ($E/\Delta E$), as simulated by *SHADOW*.

comparison, the energy-resolving power is $\sim 1.5 \times 10^4$ for the 2000 lines mm^{-1} grating.

Generally, in order to discriminate the dispersed pink beam clearly, the energy-resolving power is set at over ten times higher than that of the pink beam. As for the SASE beam, the bandwidth (root mean square, RMS) at 1033 eV is 0.04% (resolving power $E/\Delta E \simeq 2500$), just as Table 1 shows. For example, the resolving power ($E/\Delta E$) is 25 000 at 1033 eV for the 3000 lines mm^{-1} grating, about ten times higher than for the pink beam. While this value is only six times higher for the 2000 lines mm^{-1} grating. So the 3000 lines mm^{-1} grating can be optimized for the energy up to 1033 eV.

The VLS grating with a central line density of 3000 lines mm^{-1} is more suitable for the spectra diagnosis of the FEL photon-energy region from 800 to 1000 eV, as shown in Fig. 11.

For the FEL beamline, to optimize the coherence and focus spot size of the incident beam on the sample, the slope error in the tangential and sagittal directions for PM1 and PM2 is better than 0.1 μrad (RMS) and 0.3 μrad (RMS), respectively. Meanwhile, the height errors are less than 6 nm, which confirms the X-ray wavefront. The actual slope error data are shown in Fig. 12 and were added to the ray-tracing results simulated by *SHADOW*, as shown in Fig. 13.

The ray-tracing results with or without slope error are shown in Fig. 13. The pulse length (FWHM, full width at half-maximum) in the X direction is 54.29 μm when the mirror is simulated without slope error, while the FWHM in the X direction is 54.19 μm with slope error, which shows that the slope error in this spectrometer has little effect and is controlled in a reasonable range.

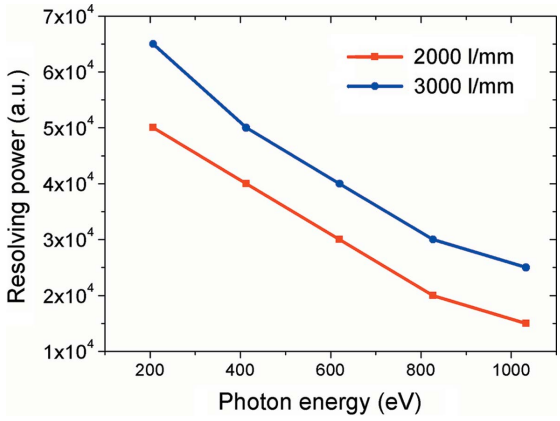

Figure 11
Energy-resolving power for the 2000 lines mm^{-1} and 3000 lines mm^{-1} gratings between the photon energies from 207 to 1033 eV.

In addition, the *SRW* code, which is based on the cross-platform wave optics, is used to detect how the height error of mirrors affects the wavefront of the X-ray radiation. Fig. 14 shows the ray-tracing results simulated by *SRW* without the height error of the radiation at PM1 and PM2, and the phase information of the wavefront is also shown.

Compared with the above simulation results, the ray-tracing results with height-error data added are shown in Fig. 15. As can be seen from the intensity and phase image, height error has a slight effect on the wavefront of the X-ray radiation at PM1. Because of the effect of height error of less than 6 nm, the propagation direction of the incident X-ray beam on PM1 will be modified accordingly. Comparing with Fig. 14(*a*), the wavefront vibration of X-ray footprint on PM1 in a tangential

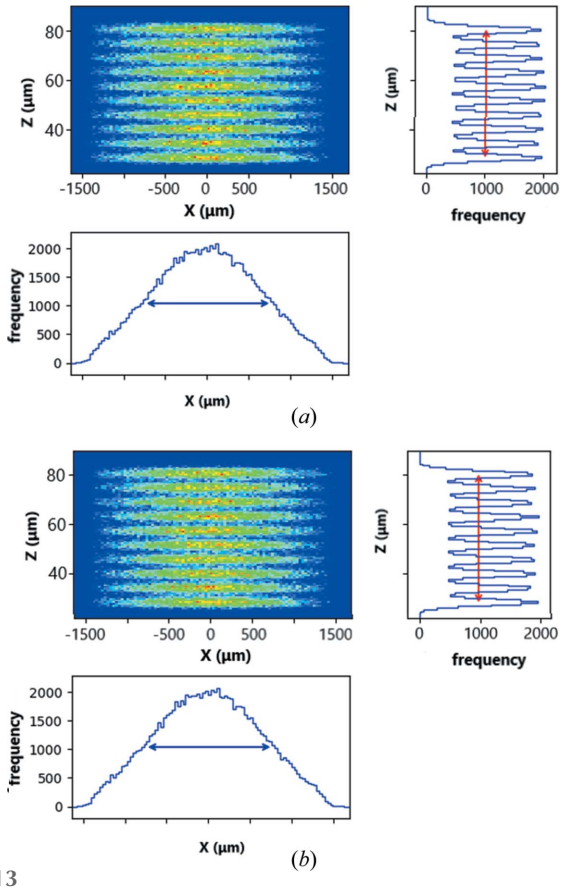

Figure 13
Ray-tracing results comparison between the results of ray tracing at the grating at 620 eV and those with an energy-resolving power of $E/\Delta E = 3 \times 10^4$ simulated by *SHADOW*. (*a*) Without slope error and (*b*) with slope error.

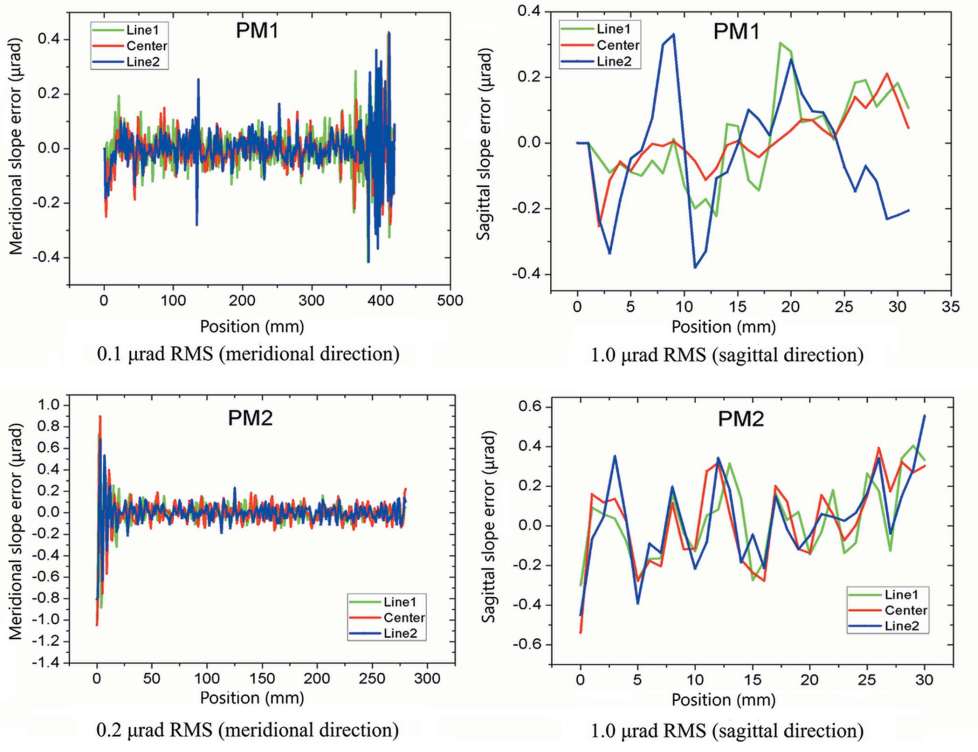

Figure 12
The actual slope error data of PM1 and PM2 in the meridional and sagittal directions.

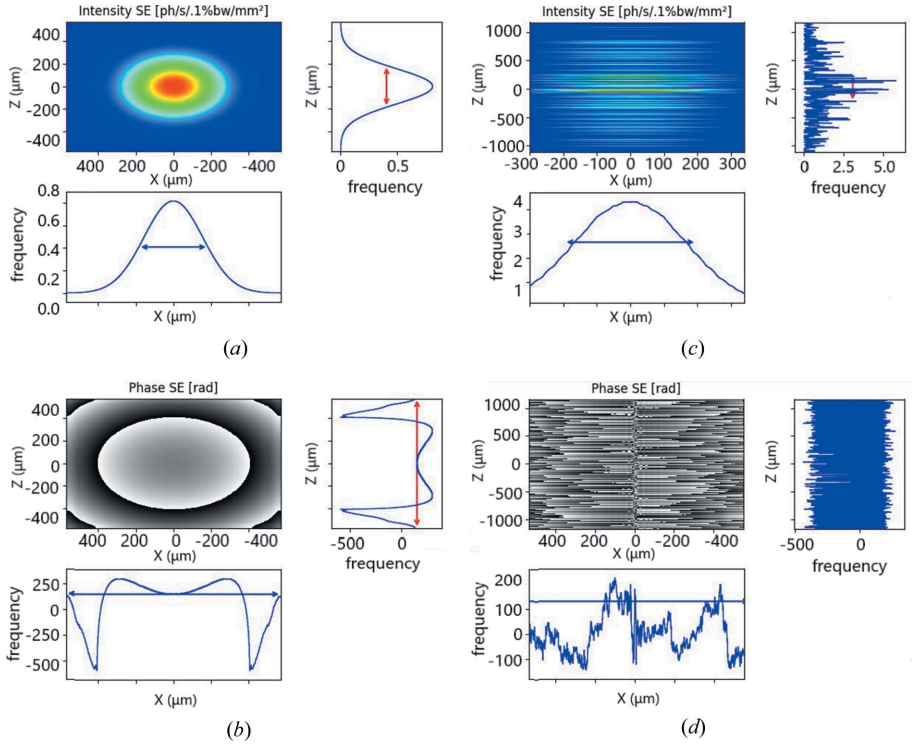

Figure 14
Ray-tracing results of PM1 and PM2 without height error, simulated by *SRW*. (*a*) Intensity of radiation at PM1, (*b*) phase of radiation at PM1, (*c*) intensity of radiation at PM2 and (*d*) phase of radiation at PM2.

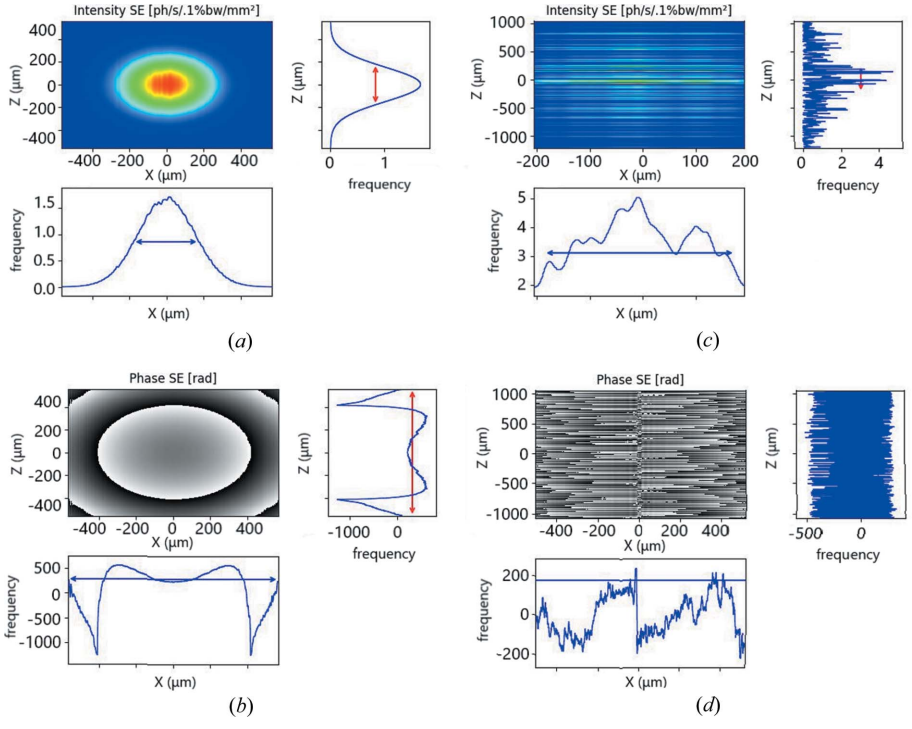

Figure 15
Ray-tracing results of PM1 and PM2 with height error, simulated by *SRW*. (*a*) Intensity of radiation at PM1, (*b*) phase of radiation at PM1, (*c*) intensity of radiation at PM2 and (*d*) phase of radiation at PM2.

direction exhibits a magnitude of 6% and a period of 20 μm, which will ultimately accumulate this effect on the wavefront distortion of the focusing spot on the sample. Relatively, the height error has more of an effect at the grating (PM2), which can be seen explicitly from the frequency of intensity in the sagittal direction of PM2. There are several ups and downs in the frequency distribution curve, and the attenuation of the wavefront is ∼40% against the ideal case. Besides, according to Figs. 14(*c*) and 15(*c*), the effect of height error on the energy-resolving power is not significant.

Finally, the first-order diffraction angle β, the exit-arm length r_2, and the tilt angle θ between the focal plane and the diffraction arm are shown in Figs. 16(*a*), 16(*b*) and 16(*c*), respectively. For the 2000 lines mm^{-1} grating, β increases monotonously from 77.12 to 85.69° with photon energy increasing from 100 to 1000 eV, r_2 increases from 3.69 to 4.21 m and θ decreases monotonously from 76.38 to 14.19°. To discriminate the adjacent dispersive lines of the energy-resolving power, the angle between the detector plane and the diffraction beam should be adjusted accordingly versus photon energy variation, as shown in Fig. 17(*a*). Fig 17(*b*) shows the actual angle-calibration system which has already been installed at SXFEL.

6. Conclusions

In summary, an online VLS grating spectrometer used as a diagnostic tool that allows noninvasive measurement of FEL radiation on a single-shot basis is presented in this work. The spectrometer consists of a plane mirror and plane VLS grating. As a result, the spectrometer diffracts only a small fraction of FEL radiation for FEL spectral analysis and deflects more than 95% of the radiation to the end station in the experiments. Simultaneously, a movable CCD camera with a motor-drive system is placed at the focal point to record the pulse spectrum. In addition, the radiation damage of B_4C compared with Au is discussed, and the results show that it is safer to use B_4C as

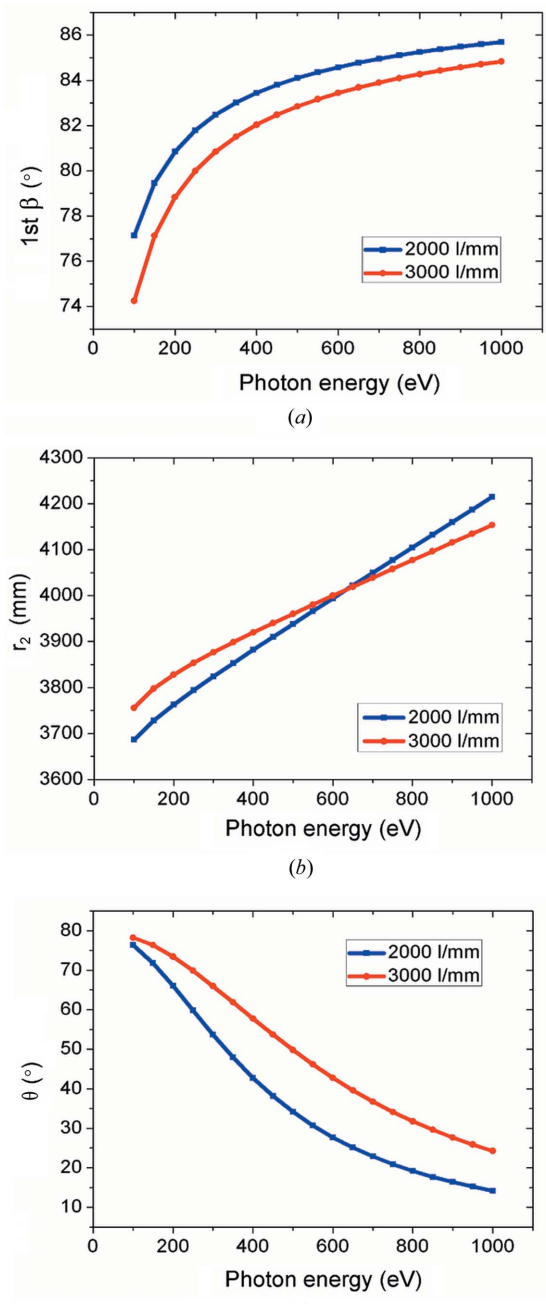

Figure 16
The functions of photon energy with (*a*) β, (*b*) r_2 and (*c*) θ of the 2000 lines mm^{-1} grating and 3000 lines mm^{-1} grating.

the coating material because the absorption dose of the single atoms of B_4C is lower than 0.1 eV atom^{-1} (safety threshold dose). The first-order diffraction efficiency of the B_4C-coated grating at 620 eV is ∼18% when the suitable ratio of the grooving width to the spacing is 0.65 and the grooving depth is 6 nm.

Meanwhile, to understand the spectral characteristics, the method of ray tracing is used for monitoring the incident radiation, and the simulation tools of *SHADOW* and *SRW* are implemented in the design of spectral diagnostic grating in the SASE FEL beamline. The energy of 620 eV is chosen as the main ray-tracing simulation energy. The ray-tracing results of

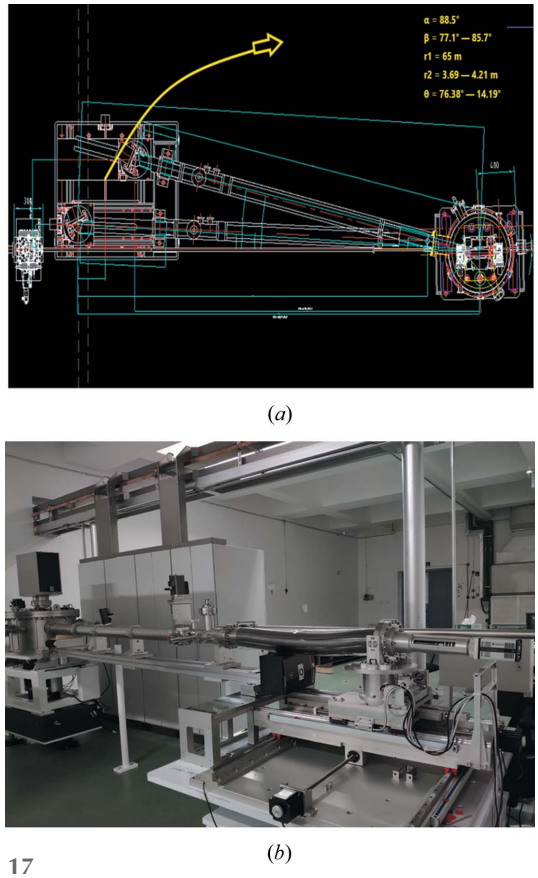

Figure 17
(*a*) Schematic of the angle-calibration system. (*b*) The installed angle-calibration system.

the spectrometer at 620 eV with a resolving power of 3×10^4 ($E/\Delta E$) simulated by both *SHADOW* and *SRW* are presented, and the interval between two adjacent energy lines is ∼5 µm.

Furthermore, based on the ray-tracing results of the gratings, the energy-resolving power for the 2000 lines mm^{-1} and 3000 lines mm^{-1} gratings is over 3×10^4 at 620 eV($E/\Delta E$). In comparison, the energy-resolving power of the 3000 lines mm^{-1} grating is higher at the photon-energy region from 800 to 1000 eV than the 2000 lines mm^{-1} grating. The energy-resolving power of the 3000 lines mm^{-1} grating can exceed 2.5×10^4 at 1033 eV. In comparison, it is ∼1.5×10^4 for the 2000 lines mm^{-1} grating. However, if considering the diffraction efficiency, the 2000 lines mm^{-1} grating is preferable to be implemented in this SASE beamline. On the other hand, the VLS grating with a central line density of 3000 lines mm^{-1} is more suitable for the spectral diagnosis of the FEL photon-energy region from 800 to 1000 eV, which provides inspiration for the future optimization of the spectrometer for the energy region from 800 to 1000 eV.

Moreover, the actual slope error data of PM1 and PM2 were added to the ray-tracing simulation and have been shown to have little effect on the focus characteristics.

Finally, for the 2000 lines mm^{-1} and 3000 lines mm^{-1} gratings, the first-order diffraction angle, the exit-arm length and the tilt angle between the focal plane and the diffraction arm

vary linearly with photon energy increasing from 100 to 1000 eV, and the angle between the detector plane and the diffraction beam should be adjusted accordingly with varying photon energy to discriminate the adjacent dispersive lines of the energy-resolving power.

The design of diagnostic spectrometers with high precision has been fulfilled, and the spectrometer has been installed and tested off-line. The mechanical and controlling systems are reliable. This work has provided comprehensive designing methods and detailed data for the design of high-precision and highly reliable diagnostic spectrometers in soft X-ray free-electron lasers and will be extremely useful for the future design of diagnostic spectrometers in other free-electron instruments.

Acknowledgements

The authors would like to thank researcher Zhi Guo and researcher Xiangyu Meng for abundant advice, and the Shanghai Synchrotron Radiation Facility for help with the equipment. Writing assistance was provided by the American Journal Experts.

Funding information

This work was supported by the National Natural Science Foundation of China (NSFC) (U1732268), the Shanghai-XFEL Beamline Project (SBP) (31011505505885920161A210-1001), the National Basic Research Program of China (973 Program) (2016YFB0700404), and NSFC (11575284).

References

Allaria, E., Appio, R., Badano, L., Barletta, W. A., Bassanese, S., Biedron, S. G., Borga, A., Busetto, E., Castronovo, D., Cinquegrana, P., Cleva, S., Cocco, D., Cornacchia, M., Craievich, P., Cudin, I., D'Auria, G., Dal Forno, M., Danailov, M. B., De Monte, R., De Ninno, G., Delgiusto, P., Demidovich, A., Di Mitri, S., Diviacco, B., Fabris, A., Fabris, R., Fawley, W., Ferianis, M., Ferrari, E., Ferry, S., Froehlich, L., Furlan, P., Gaio, G., Gelmetti, F., Giannessi, L., Giannini, M., Gobessi, R., Ivanov, R., Karantzoulis, E., Lonza, M., Lutman, A., Mahieu, B., Milloch, M., Milton, S. V., Musardo, M., Nikolov, I., Noe, S., Parmigiani, F., Penco, G., Petronio, M., Pivetta, L., Predonzani, M., Rossi, F., Rumiz, L., Salom, A., Scafuri, C., Serpico, C., Sigalotti, P., Spampinati, S., Spezzani, C., Svandrlik, M., Svetina, C., Tazzari, S., Trovo, M., Umer, R., Vascotto, A., Veronese, M., Visintini, R., Zaccaria, M., Zangrando, D. & Zangrando, M. (2012). *Nat. Photon.* **6**, 699–704.

Amann, J., Berg, W., Blank, V., Decker, F.-J., Ding, Y., Emma, P., Feng, Y., Frisch, J., Fritz, D., Hastings, J., Huang, Z., Krzywinski, J., Lindberg, R., Loos, H., Lutman, A., Nuhn, H.-D., Ratner, D., Rzepiela, J., Shu, D., Shvyd'ko, Yu., Spampinati, S., Stoupin, S., Terentyev, S., Trakhtenberg, E., Walz, D., Welch, J., Wu, J., Zholents, A. & Zhu, D. (2012). *Nat. Photon.* **6**, 693–698.

Ayvazyan, V., Baboi, N., Bähr, J., Balandin, V., Beutner, B., Brandt, A., Bohnet, I., Bolzmann, A., Brinkmann, R., Brovko, O. I., Carneiro, J. P., Casalbuoni, S., Castellano, M., Castro, P., Catani, L., Chiadroni, E., Choroba, S., Cianchi, A., Delsim-Hashemi, H., Di Pirro, G., Dohlus, M., Düsterer, S., Edwards, H. T., Faatz, B., Fateev, A. A., Feldhaus, J., Flöttmann, K., Frisch, J., Fröhlich, L., Garvey, T., Gensch, U., Golubeva, N., Grabosch, H.-J., Grigoryan, B., Grimm, O., Hahn, U., Han, J. H., Hartrott, M. V., Honkavaara, K., Hüning, M., Ischebeck, R., Jaeschke, E., Jablonka, M., Kammering, R., Katalev, V., Keitel, B., Khodyachykh, S., Kim, Y., Kocharyan, V., Körfer, M., Kollewe, M., Kostin, D., Krämer, D., Krassilnikov, M., Kube, G., Lilje, L., Limberg, T., Lipka, D., Löhl, F., Luong, M., Magne, C., Menzel, J., Michelato, P., Miltchev, V., Minty, M., Möller, W. D., Monaco, L., Müller, W., Nagl, M., Napoly, O., Nicolosi, P., Nölle, D., Nuñez, T., Oppelt, A., Pagani, C., Paparella, R., Petersen, B., Petrosyan, B., Pflüger, J., Piot, P., Plönjes, E., Poletto, L., Proch, D., Pugachov, D., Rehlich, K., Richter, D., Riemann, S., Ross, M., Rossbach, J., Sachwitz, M., Saldin, E. L., Sandner, W., Schlarb, H., Schmidt, B., Schmitz, M., Schmüser, P., Schneider, J. R., Schneidmiller, E. A., Schreiber, H.-J., Schreiber, S., Shabunov, A. V., Sertore, D., Setzer, S., Simrock, S., Sombrowski, E., Staykov, L., Steffen, B., Stephan, F., Stulle, F., Sytchev, K. P., Thom, H., Tiedtke, K., Tischer, M., Treusch, R., Trines, D., Tsakov, I., Vardanyan, A., Wanzenberg, R., Weiland, T., Weise, H., Wendt, M., Will, I., Winter, A., Wittenburg, K., Yurkov, M. V., Zagorodnov, I., Zambolin, P. & Zapfe, K. (2006). *Eur. Phys. J. D*, **37**, 297–303.

Ayvazyan, V., Baboi, N., Bohnet, I., Brinkmann, R., Castellano, M., Castro, P., Catani, L., Choroba, S., Cianchi, A., Dohlus, M., Edwards, H. T., Faatz, B., Fateev, A. A., Feldhaus, J., Flöttmann, K., Gamp, A., Garvey, T., Genz, H., Gerth, Ch., Gretchko, V., Grigoryan, B., Hahn, U., Hessler, C., Honkavaara, K., Hüning, M., Ischebeck, R., Jablonka, M., Kamps, T., Körfer, M., Krassilnikov, M., Krzywinski, J., Liepe, M., Liero, A., Limberg, T., Loos, H., Luong, M., Magne, C., Menzel, J., Michelato, P., Minty, M., Müller, U.-C., Nölle, D., Novokhatski, A., Pagani, C., Peters, F., Pflüger, J., Piot, P., Plucinski, L., Rehlich, K., Reyzl, I., Richter, A., Rossbach, J., Saldin, E. L., Sandner, W., Schlarb, H., Schmidt, G., Schmüser, P., Schneider, J. R., Schneidmiller, E. A., Schreiber, H.-J., Schreiber, S., Sertore, D., Setzer, S., Simrock, S., Sobierajski, R., Sonntag, B., Steeg, B., Stephan, F., Sytchev, K. P., Tiedtke, K., Tonutti, M., Treusch, R., Trines, D., Türke, D., Verzilov, V., Wanzenberg, R., Weiland, T., Weise, H., Wendt, M., Will, I., Wolff, S., Wittenburg, K., Yurkov, M. V. & Zapfe, K. (2002). *Phys. Rev. Lett.* **88**, 104802.

Bahrdt, J. (2007). *Phys. Rev. ST Accel. Beams*, **10**, 060701.

Bionta, R. M. (2000). *LCLS Technical Note*. No. LCLS-TN-00-3. LCLS, SLAC National Accelerator Laboratory, Menlo Park, CA, USA.

Brenner, G., Kapitzki, S., Kuhlmann, M., Ploenjes, E., Noll, T., Siewert, F., Treusch, R., Tiedtke, K., Reininger, R., Roper, M. D., Bowler, M. A., Quinn, F. M. & Feldhaus, J. (2011). *Nucl. Instrum. Methods Phys. Res. A*, **635**, S99–S103.

Chubar, O. (2014). *Proc. SPIE*, **9209**, 920907.

Chubar, O., Berman, L., Chu, Y., Fluerasu, A., Hulbert, S., Idir, M., Kaznatcheev, K., Shapiro, D., Shen, Q. & Baltser, J. (2011). *Proc. SPIE*, **8141**, 814107.

Emma, P., Akre, R., Arthur, J., Bionta, R., Bostedt, C., Bozek, J., Brachmann, A., Bucksbaum, P., Coffee, R., Decker, F.-J., Ding, Y., Dowell, D., Edstrom, S., Fisher, A., Frisch, J., Gilevich, S., Hastings, J., Hays, G., Hering, Ph., Huang, Z., Iverson, R., Loos, H., Messerschmidt, M., Miahnahri, A., Moeller, S., Nuhn, H.-D., Pile, G., Ratner, D., Rzepiela, J., Schultz, D., Smith, T., Stefan, P., Tompkins, H., Turner, J., Welch, J., White, W., Wu, J., Yocky, G. & Galayda, J. (2010). *Nat. Photon.* **4**, 641–647.

Frassetto, F., Cocco, D., Zangrando, M. & Poletto, L. (2008). *Nucl. Instrum. Methods Phys. Res. A*, **593**, 129–131.

Guo, Z., Meng, X., Wang, Y., Liu, H., Zhang, X., Li, Z., Xue, L. & Tai, R. (2017). *J. Synchrotron Rad.* **24**, 877–885.

Harada, T. & Kita, T. (1980). *Appl. Opt.* **19**, 3987–3993.

Harada, T., Takahashi, K., Sakuma, H. & Osyczka, A. (1999). *Appl. Opt.* **38**, 2743–2748.

Kita, T., Harada, T., Nakano, N. & Kuroda, H. (1983). *Appl. Opt.* **22**, 512–513.

Koyama, T., Yumoto, H., Miura, T., Tono, K., Togashi, T., Inubushi, Y., Katayama, T., Kim, J., Matsuyama, S., Yabashi, M., Yamauchi, K. & Ohashi, H. (2016). *Rev. Sci. Instrum.* **87**, 051801.

Li, C., Wei, S., Du, X., Du, L., Wang, Q., Zhang, W., Wu, G., Dai, D. & Yang, X. (2015). *Nucl. Instrum. Methods Phys. Res. A*, **783**, 65–67.
Makita, M., Karvinen, P., Zhu, D., Juranic, P. N., Grünert, J., Cartier, S., Jungmann-Smith, J. H., Lemke, H. T., Mozzanica, A., Nelson, S., Patthey, L., Sikorski, M., Song, S., Feng, Y. & David, C. (2015). *Optica*, **2**, 912–916.
McNeil, B. W. J. & Thompson, N. R. (2010). *Nat. Photon.* **4**, 814–821.
Meng, X., Guo, Z., Wang, Y., Zhang, H., Han, Y., Zhao, G., Liu, Z. & Tai, R. (2019). *J. Synchrotron Rad.* **26**, 543–550.
Meng, X., Shi, X., Wang, Y., Reininger, R., Assoufid, L. & Tai, R. (2017). *J. Synchrotron Rad.* **24**, 954–962.
Noda, H., Namioka, T. & Seya, M. (1974). *J. Opt. Soc. Am.* **64**, 1031–1036.
Palutke, S., Gerken, N. C., Mertens, K., Klumpp, S., Mozzanica, A., Schmitt, B., Wunderer, C., Graafsma, H., Meiwes-Broer, K.-H., Wurth, W. & Martins, M. (2015). *Rev. Sci. Instrum.* **86**, 113107.
Rehanek, J., Makita, M., Wiegand, P., Heimgartner, P., Pradervand, C., Seniutinas, G., Flechsig, U., Thominet, V., Schneider, C. W., Fernandez, A. R., David, C., Patthey, L. & Juranić, P. (2017). *J. Instrum.* **12**, P05024.
Reininger, R., Feldhaus, J., Plönjes, E., Treusch, R., Roper, M. D., Quinn, F. M. & Bowler, M. A. (2004). *AIP Conf. Proc.* **705**, 572–575.
Saldin, E. L., Schneidmiller, E. A. & Yurkov, M. V. (1995). *Phys. Rep.* **260**, 187–327.
Samoylova, L., Buzmakov, A., Geloni, G., Chubar, O. & Sinn, H. (2011). *Proc. SPIE*, **8141**, 81410A.
Sanchez del Rio, M., Canestrari, N., Jiang, F. & Cerrina, F. (2011). *J. Synchrotron Rad.* **18**, 708–716.
Stohr, J. (2011). *Linac Coherent Light Source II Conceptual Design Report.* SLAC-I-060-003-000-00. SLAC National Accelerator Laboratory, Meno Park, CA, USA.
Svetina, C., Cocco, D., Mahne, N., Raimondi, L., Ferrari, E. & Zangrando, M. (2016). *J. Synchrotron Rad.* **23**, 35–42.
Thompson, A. C. & Vaughan, D. (2001). *X-ray Data Booklet*, 2nd ed., ch. 4.2, pp. 1–5.
Tiedtke, K., Feldhaus, J., Gerth, Ch., Hahn, U., Jastrow, U., Ploenjes, E., Steeg, B. & Treusch, R. (2004). *AIP Conf. Proc.* **705**, 588.
Togashi, T., Takahashi, E. J., Midorikawa, K., Aoyama, M., Yamakawa, K., Sato, T., Iwasaki, A., Owada, S., Yamanouchi, K., Hara, T., Matsubara, S., Ohshima, T., Otake, Y., Tamasaku, K., Tanaka, H., Tanaka, T., Tomizawa, H., Watanabe, T., Yabashi, M. & Ishikawa, T. (2013). *Radiat. Phys. Chem.* **93**, 25–32.
Tono, K., Togashi, T., Inubushi, Y., Sato, T., Katayama, T., Ogawa, K., Ohashi, H., Kimura, H., Takahashi, S., Takeshita, K., Tomizawa, H., Goto, S., Ishikawa, T. & Yabashi, M. (2013). *New J. Phys.* **15**, 083035.
Yabashi, M., Higashiya, A., Tamasaku, K., Kimura, H., Kudo, T., Ohashi, H., Takahashi, S., Goto, S. & Ishikawa, T. (2007). *Proc. SPIE*, **6586**, 658605.